A 3D scanning system for biomedical purposes

B.D. Bradley and A.D.C. Chan*

Faculty of Engineering and Design,
Department of Systems and Computer Engineering,
Carleton University,
1125 Colonel By Dr. Ottawa, K1S 5B6 ON, Canada
E-mail: bbradley@sce.carleton.ca
E-mail: adcchan@sce.carleton.ca
*Corresponding author

M.J.D. Hayes

Faculty of Engineering and Design,
Department of Mechanical and Aerospace Engineering,
Carleton University,
1125 Colonel By Dr. Ottawa, K1S 5B6 ON, Canada
E-mail: jhayes@mae.carleton.ca

Abstract: The use of three-dimensional (3D) scanning systems for acquiring the external shape features of biological objects has recently been gaining popularity in the biomedical field. A simple, low cost, 3D scanning system is presented, which employs the laser light-sectioning technique for data acquisition. A Direct Linear Transformation least squares algorithm is used for camera calibration and Elliptical Fourier Descriptors (EFDs) are used for data smoothing and planar section reconstruction. Results for an experiment demonstrating the validity of the EFD approach are presented. Overall, results presented for three objects scanned with the proposed system demonstrate the validity of the chosen approach.

This is an expanded version of a paper presented at the 3rd IEEE International Workshop on Medical Measurements and Applications, 9–10 May 2008, Ottawa, ON, Canada.

Keywords: 3D geometric modelling; 3D scanning; laser light-sectioning; biomedical scanner; EFDs; elliptical fourier descriptors; camera calibration; direct linear transformation.

Reference to this paper should be made as follows: Bradley, B.D., Chan, A.D.C. and Hayes, M.J.D. (2009) 'A 3D scanning system for biomedical purposes', *Int. J. Advanced Media and Communication*, Vol. 3, Nos. 1/2, pp.35–54.

Biographical notes: Beverly D. Bradley received her BASc Degree in Systems Design Engineering from the University of Waterloo, Waterloo, ON, Canada in 2006. In 2008, she completed her MASc in Biomedical Engineering at Carleton University, Ottawa, ON, Canada, where she specialised in medical instrumentation. She is currently working for the Biomedical Engineering department at MRC Laboratories in The Gambia, West Africa.

Adrian D.C. Chan received a BASc Degree in Computer Engineering from the University of Waterloo, Waterloo, ON, Canada, in 1997, a MASc Degree in Electrical Engineering from the University of Toronto, Toronto, ON, Canada in 1999, and a PhD Degree in Electrical Engineering from the University of New Brunswick, Fredericton, NB, Canada in 2003. He is currently an Associate Professor with the Department of Systems and Computer Engineering, Carleton University, Ottawa, ON, Canada. His research interests include biological signal processing, pattern recognition, assistive devices, noninvasive sensors, and electronic noses.

M. John D. Hayes received his BEng (1995), MEng (1996), and PhD (1999) Degrees all from McGill University in Montreal, QC, Canada. He is currently an Associate Professor in the Department of Mechanical and Aerospace Engineering at Carleton University in Ottawa, ON, Canada. His research interests include computational kinematics, algebraic geometry, and optimisation as they apply to robot mechanical systems, machine vision, and medical devices.

1 Introduction

The use of three-dimensional (3D) scanning systems for acquiring 3D models of objects has many applications in industry, computer graphics, and more recently, medicine. Biomedical applications of 3D scanning include orthodontic treatment planning (Hajeer et al., 2004), anatomical parts reconstruction (Tognola et al., 2003a), cranial deformation research (Hennessey et al., 2005), cartilage morphology studies (Trinh et al., 2006), and anthropometric data collection (Azouz et al., 2005). There exists a variety of different techniques for acquiring 3D models of objects, all with a wide range of hardware costs, and differing levels of achievable accuracy and detail in the captured geometric models. Good reviews of 3D model acquisition techniques and the processing of scanner output into 3D models have been prepared by Bernardini and Rushmeier (2002) and Curless (1999). In medical applications, one typically thinks of Computed Tomography (CT) and Magnetic Resonance Imaging (MRI) as modes of acquiring 3D information; these are both extremely expensive to operate, and in the case of CT, expose patients to harmful ionising radiation rendering it unsuitable for routine procedures. For certain biomedical applications where only the external 3D geometry of an object is desired, 3D laser scanners are becoming a viable and efficient means of capturing 3D information.

Although there currently exist numerous commercial laser scanning systems,

> "in order to apply surface scanners in medicine, one usually has to resort to commercially produced systems originally designed for industrial use." (Schwenzer-Zimmerer et al., 2008, p.59)

Despite the fact that

> "these devices can be considered as the state of the art of scanning technology for their remarkable accuracy, resolution, and velocity, they may present some limitations [when adopted for biomedical applications]." (Tognola et al., 2003b, p.295)

Possible sources of error in the clinical use of the scanning technology have to be investigated; for example, the special characteristics of vital tissues (e.g., great

variations in texture, tension, transparency, and reflectivity) which are rarely encountered in artificial objects (Kovacs et al., 2006). Also, measurement errors due to patient movement, even just from breathing, are inevitable. This implies that the accuracy levels some scanners are capable of attaining (sometimes at a micron level) are not realistically achieved in a medical scenario (Boehnen and Flynn, 2005). As well, although they are relatively less expensive than CT or MRI, many scanners are still prohibitively expensive for widespread use in medical institutions.

The objective set out for this research is to develop a simple, low cost, 3D scanning system intended for biomedical purposes. We have decided to focus upon the accepted technique of laser light-sectioning for this scanner. Since cost is often a major roadblock in many healthcare institutions, this was a key constraint for this research. By including more complexity in signal processing and analysis, the use of simple, inexpensive, off-the-shelf components lends itself to a more economical design with a straightforward setup. Automation of the acquisition process was done to help reduce the need for user intervention. Finally, since the complexity (and cost) of many commercial scanners increases in order to produce highly accurate data, and since noise in measurement data is inevitable in many biomedical scenarios, we examined reliable and robust data processing options which would address noise in the measurement data and which would be particularly suited for biological objects.

2 Proposed approach

2.1 The laser light-sectioning technique

As mentioned in the introduction, we have decided to focus upon the accepted technique of laser light-sectioning for this system. This technique involves measuring the position of an object's surface profile by recording where the profile intersects a plane of laser light projected onto the object from different angles (Figure 1). A single planar section of an object is obtained from multiple profiles captured about the z-axis. A 3D image of the object is formed by stacking multiple planar sections along the z-axis.

Figure 1 Laser light-sectioning system diagram (see online version for colours)

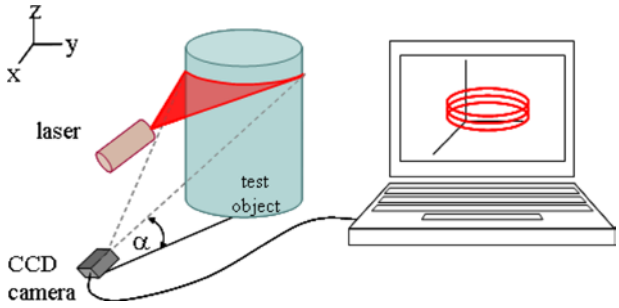

Two main challenges exist when using this technique. First, since the camera used is located at a fixed angle to the laser plane, the images contain perspective distortion which must be compensated for. We refer to this as the calibration problem.

Second, when employing the laser light-sectioning technique, only a portion of the object's profile can be captured from any given angle. Therefore the object model must be reconstructed by aligning numerous segments of data into a complete planar contour before stacking multiple contours to form the 3D representation. We refer to this as the data manipulation problem. Although there are many other aspects involved with this imaging technique (as will be discussed in Section 2.3), the work presented here focuses on these two main challenges.

2.2 System hardware setup

The system setup is illustrated in Figure 2. A Stockeryale (Montreal, PQ) Lasiris SNF635S-5 Class IIIa Diode Laser fitted with line-generating optics creates a horisontal light plane (i.e., parallel to the xy-plane). The trace of the light plane is visible when projected onto the object of interest and is recorded with a JAI Pulnix (San Jose, CA) TM-200 High Resolution (768×494) Charge-Coupled Device (CCD) camera. Both are mounted to a platform; the camera is inclined at $\alpha = 30°$. This angle was chosen to gain a larger measurement range in order to be able to scan objects with larger variations in surface topography, even though resolution is slightly reduced with a smaller angle (Lichtschnitt, 2004).

Figure 2 Prototype setup (see online version for colours)

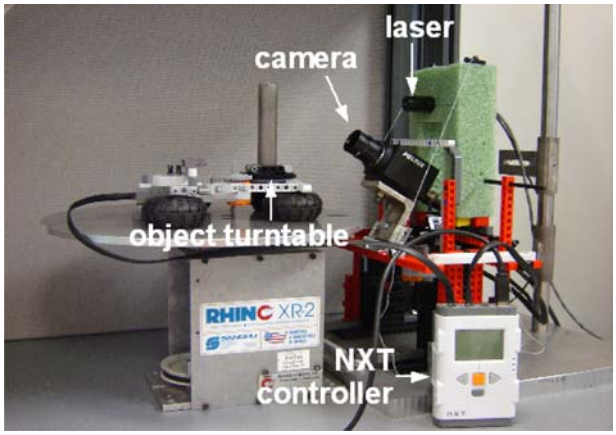

The object to be scanned is placed on a turntable approximately 10 cm from the camera. Images are captured with a National Instruments (NI) (Austin, TX) PCI-1411 image acquisition device. Servo motors are used to move the camera/laser platform vertically and to rotate the turntable in fixed increments. Motors are controlled with the Lego NXT controller box (32-bit ARM7 microcontroller, 256 Kbytes FLASH, 64 Kbytes RAM), which interfaces to the computer (and Labview) via USB. A single Labview (NI) program is used to control the entire system (i.e., the servo motors and the image capture device). Matlab is used for offline processing of the images and data. The computer used is a 3 GHz Pentium 4 with 1 GB RAM running Windows XP Professional.

Total estimated cost of the system (camera, laser, image acquisition device, motors and mechanical setup) is approximately $2800 USD.

2.3 Image acquisition and data processing

The general image acquisition and data processing steps for obtaining a reconstruction of the exterior features of an object are:

- *Calibration*: The system must first undergo a calibration procedure to determine a transformation matrix H which will compensate for the projective distortion of the camera.
- *Image acquisition*: M views of the laser trace on the object are then captured, separated by rotations of $R = \frac{360^\circ}{M}$ about the vertical z-axis. This process is repeated for N_z planar cross-sections in vertical increments along the z-axis.
- *Image processing*: Images undergo processing in order to isolate the laser trace segments within the image, and determine a set of point coordinates to represent the trace.
- *Data manipulation*: Laser trace point coordinates are transformed using the transformation matrix H obtained from the calibration procedure. Then the segments are registered into a common coordinate system by rotating them to their respective orientation and stacking them along the vertical z-axis. Curve fitting is applied to the segments of each planar section to form entire 360° outlines of the external profile of the object, resulting in a 3D point cloud representing the object's surface.
- *Object reconstruction*: A 3D surface mesh is applied to the point cloud in order to reconstruct the final 3D model.

Calibration: The result of projecting a plane of laser light onto an object is an illuminated stripe where the plane intersects the object's surface. This stripe is captured in a 2D image by the camera. Since the camera used to capture images is located at a fixed angle α to the laser plane, the basic goal of calibration is to eliminate the linear portion of the resulting camera perspective distortion. In other words, we must find a mapping between the illuminated pixel coordinates of the laser trace from the image to the world coordinates of the corresponding object surface points in the xy-plane. Figure 3(a) shows the image captured by the camera if a grid were to be superimposed on the plane of the laser; the highlighted quadrilateral demonstrates the camera perspective distortion. Figure 3(b) shows how a mapping from image coordinates to real world coordinates would remove this distortion.

Figure 3 Diagram illustrating mapping between image and real world coordinates removing perspective distortion (see online version for colours)

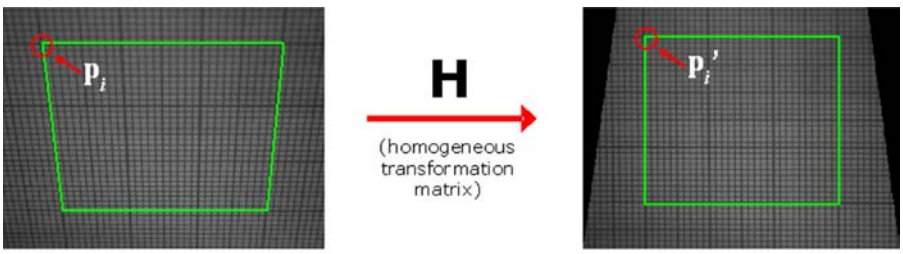

Mathematically, this transformation is represented by equation (1):

$$\mathbf{p}'_i = H\mathbf{p}_i \tag{1}$$

where H maps a point $\mathbf{p}_i = (x_i, y_i, w_i)^T$ in the image to point $\mathbf{p}'_i = (x'_i, y'_i, w'_i)^T$ in real world coordinates, effectively straightening the lines in Figure 3(a). Note the distinction between the homogeneous coordinates of a point $\mathbf{p}_i = (x_i, y_i, w_i)^T$ and the inhomogeneous coordinates $(\frac{x_i}{w_i}, \frac{y_i}{w_i})^T$; w_i in the homogeneous case represents a scale factor and not the z-coordinate, and in the inhomogeneous case the coordinates represent ratios of this factor. It should also be noted that H is a homogeneous matrix, which means that multiplying the matrix by an arbitrary non-zero scale factor will not alter the projective transformation. Consequently there are eight independent ratios amongst the nine elements of H; hence, the transformation H is specified by eight parameters. By superimposing a calibration grid on the plane of the laser as shown in Figure 3, the unknown elements of H can be determined using linear algebra and sets of corresponding control point pairs $\mathbf{p}_i \rightarrow \mathbf{p}'_i$; that is, points on the image of the calibration grid and the known corresponding points in the real world coordinate system according to the known grid dimensions.

A Least Squares (LS) approach involving the Direct Linear Transformation (DLT) algorithm is used to find the transformation matrix H. The details of the method are as follows. Expressing equation (1) as a vector cross product $\mathbf{p}'_i \times H\mathbf{p}_i = 0$ and isolating the elements of the H matrix into a column vector results in the following:

$$\begin{bmatrix} 0 & 0 & 0 & -w'_i(x_i, y_i, w_i) & y'_i(x_i, y_i, w_i) \\ w'_i(x_i, y_i, w_i) & 0 & 0 & 0 & -x'_i(x_i, y_i, w_i) \end{bmatrix} \mathbf{h} = \mathbf{0}, \tag{2}$$

where $\mathbf{h} = (h_1, h_2, \ldots, h_9)^T$ are the nine elements of the matrix H, and the third equation has been removed as only the first two are linearly independent. The 2×9 matrix of equation (2) is denoted as A_i, and the whole expression is referred to as the DLT matrix equations for the ith point correspondence.

For the specific case of laser light-sectioning calibration, an inhomogeneous case of the DLT algorithm is used. This means, rather than solve for $\mathbf{h}$ directly as a homogeneous vector, we can impose that one of the nine elements of H (say, H_{33} and thus h_9) be 1, leaving eight independent ratios amongst the nine elements of H to be found. The result is the inhomogeneous set of linear equations, given in equation (3):

$$\begin{bmatrix} 0 & 0 & 0 & x_i w'_i & y_i w'_i & w_i w'_i & -x_i y'_i & -y_i y'_i \\ x_i w'_i & y_i w'_i & w_i w'_i & 0 & 0 & 0 & -x_i x'_i & -y_i x'_i \end{bmatrix} \tilde{\mathbf{h}} = \begin{pmatrix} w_i y'_i \\ w_i x'_i \end{pmatrix}, \tag{3}$$

where $\tilde{\mathbf{h}}^T$ is a 1×8 inhomogeneous vector consisting of the first eight components of $\mathbf{h}$. Furthermore, since the DLT equations hold for any homogeneous representation (x'_i, y'_i, w'_i) of the point $\mathbf{p}'_i$ a further simplification in the laser light-sectioning calibration case is to set $w'_i = 1$ and $w_i = 1$; this means (x'_i, y'_i) and (x_i, y_i) are the 2D world coordinates and the 2D image coordinates, respectively. Thus, equation (3) simplifies to:

$$\begin{bmatrix} 0 & 0 & 0 & x_i(1) & y_i(1) & w_i(1) & -x_i y'_i & -y_i y'_i \\ x_i(1) & y_i(1) & w_i(1) & 0 & 0 & 0 & -x_i x'_i & -y_i x'_i \end{bmatrix} \tilde{\mathbf{h}} = \begin{pmatrix} y'_i \\ x'_i \end{pmatrix}. \tag{4}$$

Since each set of control point pairs gives two such equations, $2m$ equations are obtained from m calibration point pairs. Concatenating the equations from $m \geq 4$ correspondences then generates a matrix equation of the form: $A_{2m\times 8}\tilde{\mathbf{h}}_{8\times 1} = \mathbf{b}_{2m\times 8}$; where A now has eight columns, $\tilde{\mathbf{h}}$ is the column vector of H matrix parameters and $\mathbf{b}$ is a 1×8 array of known calibration coordinates. If $m > 4$, such an over-determined system can be solved for $\tilde{\mathbf{h}}$ with least squares methods.

Previous work (Bradley et al., 2008) compared this approach with a purely analytical technique, analysing the ability of each method to cope with noise in the input data (i.e., the control points selected from the image of the calibration grid). It was found that the DLT LS approach performed significantly better than the analytical technique when more than 20 point correspondences are used for computing H, and so it is the method used for this work.

Figure 4 shows a plot of average error vs. number of point correspondences used in the DLT LS method at a noise level of $\sigma^2 = 2.25$ (the expected level of noise in input data for this calibration scenario). Clearly, as the number of points used with the DLT LS method increases, average error decreases. The difference in average error obtained when using 24 points compared to four points is 0.0925 mm whereas the difference in average error obtained when using 48 points compared to 24 is only 0.0239 mm; the improvement in error in the later case is almost four times less compared to the first. While the amount of improvement in error reduces with each additional point, the additional points do not add a significant amount of time to the entire calibration process (DLT processing times < 2 ms) and may be worth the benefit gained in terms of error reduction.

Figure 4 Average error vs. number of points used with the DLT LS method (for $\sigma^2 = 2.25$) (see online version for colours)

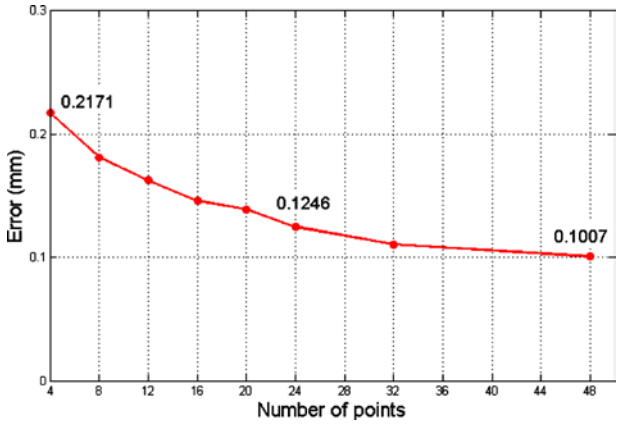

Image acquisition: For image acquisition, $M = 8$ views of the laser trace are captured by the CCD camera, separated by rotations of $R = 45°$ about the vertical z-axis. This is accomplished by placing the object on the turntable depicted in Figure 2. After images for a complete planar section have been captured, the platform holding the camera and laser is raised in increments of 2 mm.

Image processing: The goal of the image processing stage is to determine a discrete set of point coordinates to represent the laser trace. Unfortunately, the laser line

in the image is in most cases diffuse and can span multiple pixels (Ofner et al., 1999) determining a set of coordinates that best traverse this trace can thus result in quantisation error.

All images are converted to grayscale images; that is, pixel values represent intensities from 0 to 255. A background eliminating algorithm is applied to the images to help isolate the laser line traces. A Centre Of Gravity (COG) approach (Ofner et al., 1999) is used to isolate the laser trace segments within the image, and determine a set of point coordinates to represent the trace. A threshold value is chosen using Otsu's method (Otsu, 1979). Pixels below the threshold are not considered in the COG algorithm and those above it are. Starting from the left side of the image, each column of the image is considered sequentially. The threshold value is used to scan each column; the portion of the column with intensities greater than the threshold value represents the laser trace and is used in the calculation of the COG. A one-dimensional moment, y_c, is calculated for the sub-column of pixels exceeding this threshold according to equation (5).

$$y_c = \frac{\sum_{y=y_s}^{y_e} y \cdot I^p(x,y)}{\sum_{y=y_s}^{y_e} I^p(x,y)}, \tag{5}$$

where x, y are coordinates in the image, $I(x,y)$ is the intensity at (x,y), y_s and y_e are the start and end indices for the column of pixels which exceed the threshold, and p is a power factor. The power factor can be used to influence the weighting of intensities; a value of $p > 1$ gives higher importance to high intensities, and $p < 1$ will emphasise pixels with lower intensities (Ofner et al., 1999). A power factor of $p = 1$ is used here, meaning the moment calculated simply corresponds to the COG. The existence of the power factor allows for extra flexibility in the formula and could be changed if the intensity of the laser trace is not very high in an image due to poor lighting conditions, etc. The point coordinate chosen to represent the centre of the laser trace then becomes (x, y_c), where x is the current column number.

The overall result of the image processing phase is that the laser traces from each image are now represented by sets of (x,y) coordinates. By transitioning from images to point coordinates, the amount of data has been substantially reduced, facilitating further manipulation in order to create a final 3D model. The end regions of the laser trace data segments tend to be plagued with noise, excessively steep slopes, and frequent outliers. This is due to the poor quality of the light signal where it intersects the outermost edges of the object (Hayes et al., 2001). For this reason, the first and last 10% of data points are discarded for the remainder of the analysis.

Data manipulation: Data are registered into a common coordinate system. First, the eight segments of each planar section are reassembled about a suitable longitudinal axis. Planar sections are then 'stacked' along this axis in the z-direction by simply introducing the appropriate increment level as the third dimension (i.e., the z-coordinate). After aligning and stacking the data segments, ideally all individual points would lie exactly on the surface of the reconstructed object. However, this is not the case due to residual error from sources, such as: noise in the measurements, inaccuracies in the camera calibration, the methodology used to obtain coordinate point data for the imaged laser traces, and imprecision in the alignment process itself (Bernardini and Rushmeier, 2002).

There are various ways to account for this residual error. Preprocessing techniques could involve removing outliers from the data, filtering the data, or fitting the individual data segments to polynomials or splines before aligning them into a seamless contour. Another approach to deal with residual error is to define new estimates of actual surface points by averaging samples from overlapping scans once they have been aligned (Bernardini and Rushmeier, 2002). Different methods of achieving this are discussed by Bernardini and Rushmeier (2002) and include techniques, such as: modelling the measurement error locally and then optimally reconstructing the object surface using the two overlapping sets of data as 'estimations' in a probabilistic sense (Rutishauser et al., 1994), and computing surface values as weighted averages of overlapping range data, where the weight used is proportional to the illuminance received by the sensor (Soucy and Laurendeau, 1995). These methods assume range input data and not necessarily data from planar laser light-sectioning.

We propose that Elliptical Fourier Descriptors (EFDs) (Khul and Giardina, 1982) are an appropriate technique for this system, both for reducing noise in the individual data segments and for fitting a single curve through the data segments. EFDs have been shown to be particularly suited for biological objects, further supporting their use for a biomedical scanner. This has been demonstrated by Jeong and Radke (2007), where they are used to fit contours of the prostate from a series of CT scans in order to construct a 3D model, and by Schmittbuhl et al. (2002), where they are used to quantify the shape of human mandibles in order to analyse variability and sexual dimorphism between individuals. A survey of many other biological applications of EFDs is presented by Lestrel (1997). We assume that for biomedical applications, surfaces being scanned will be smooth and the use of EFDs is thus appropriate. The scanning of non-smooth surfaces is beyond the scope of this work.

First, a simple method of averaging overlapping segment data was implemented whereby the section of overlapping segments is replaced by a new segment whose points are the mid-points, radially, between the two overlapping segments. As suggested by Bernardini and Rushmeier (2002), defining new estimates of actual surface points by averaging samples from overlapping scans is an approach to dealing with residual error in the data.

Secondly, for the curve fitting step of the data manipulation stage, EFDs are used to fit a smooth curve through the segments of each planar section. Khul and Giardina (1982) were the first to introduce the concepts of Elliptical Fourier Functions (EFFs) and EFDs. They proposed that a 2D continuous closed contour can be represented, parametrically, as a function of time, $V(t)$. Projections of this vector function on the x- and y-axes, represented by $x(t)$ and $y(t)$, are periodic with period T, where T is the time required to trace the entire contour at a constant speed. These projections can be represented by Fourier trigonometric series. Different levels of approximation to the closed contour represented by $x(t)$ and $y(t)$ can be obtained by truncating the EFFs after different numbers of harmonics as given by equations (6) and (7), where n equals the harmonic number and N equals the maximum harmonic number before truncation. Complex object profiles are thus represented with higher order harmonics.

$$x_N(t) = A_0 + \sum_{n=1}^{N} a_n \cos \frac{2\pi nt}{T} + \sum_{n=1}^{N} b_n \sin \frac{2\pi nt}{T}, \tag{6}$$

$$y_N(t) = C_0 + \sum_{n=1}^{N} c_n \cos\frac{2\pi nt}{T} + \sum_{n=1}^{N} d_n \sin\frac{2\pi nt}{T}. \tag{7}$$

Khul and Giardina (1982) also developed formulae for the coefficients A_0, C_0, a_n, b_n, c_n and d_n which do not require the evaluation of integrals; these are given in equations (8)–(10).

$$A_0 = \frac{1}{T}\sum_{p=1}^{K} \frac{\Delta x_p}{2\Delta t_p}(t_p^2 - t_{p-1}^2) + \xi_p(t_p - t_{p-1}), \tag{8}$$

$$a_n = \frac{T}{2\pi^2 n^2}\sum_{p=1}^{K} \frac{\Delta x_p}{\Delta t_p}\left[\cos\frac{2\pi nt_p}{T} - \cos\frac{2\pi nt_{p-1}}{T}\right], \tag{9}$$

$$b_n = \frac{T}{2\pi^2 n^2}\sum_{p=1}^{K} \frac{\Delta x_p}{\Delta t_p}\left[\sin\frac{2\pi nt_p}{T} - \sin\frac{2\pi nt_{p-1}}{T}\right], \tag{10}$$

where

$$\xi_p = \sum_{j=1}^{p-1} \Delta x_j - \frac{\Delta x_p}{\Delta t_p}\sum_{j=1}^{p-1} \Delta t_j. \tag{11}$$

Similar expressions can be derived for C_0, c_n, and d_n. EFDs are broadly defined as the 'output' from the Fourier curve fit (Lestrel, 1997) and numerically describe the contour boundary information. With these descriptors, an approximation to the original contour can be re-created at any time in the absence of the original data.

Work has been done to develop a preprocessing technique that will automatically identify an appropriate number of harmonics to use for a given set of data segments. A unique harmonic number HN is found for each planar section of data segments and is based on two parameters: the perimeter/area ratio PA for that section and a roundness factor RF. The perimeter pm for a given section is determined from the set of point coordinates for that contour by adding the distances between adjacent points. The area a is found by computing the area of the polygon formed by the set of point coordinates. PA is simply the ratio of the perimeter pm and area a. RF is a simple metric between 0 and 1, which indicates how 'round' the contour is (equation (12)). For a perfect circle, RF is 1.

$$RF = \frac{4\pi a}{pm^2}. \tag{12}$$

The harmonic number calculation for the kth section is given in equation (13) and would be rounded to the nearest integer.

$$HN_k = \frac{1}{PA_k \times RF_k}. \tag{13}$$

Figure 5 demonstrates how this harmonic calculation works for simulated data of a square, pentagon, octagon, and arbitrary blob object. The HN values calculated for

these data sets were 6, 5, 5, and 18 respectively. Because the pentagon and octagon are more 'round' than the square, they required fewer harmonics. A larger number of harmonics is expected for the blob object given its complexity in shape. While this algorithm appears to provide a reasonable harmonic number, it is not robust for objects with sharp corners; however, since the target application for this scanner will be smooth objects, it is assumed that the HN metric is sufficient for harmonic calculation in this work.

Figure 5 EFD fit using calculated HN for: (a) square; (b) pentagon; (c) octagon and (d) arbitrary blob object (see online version for colours)

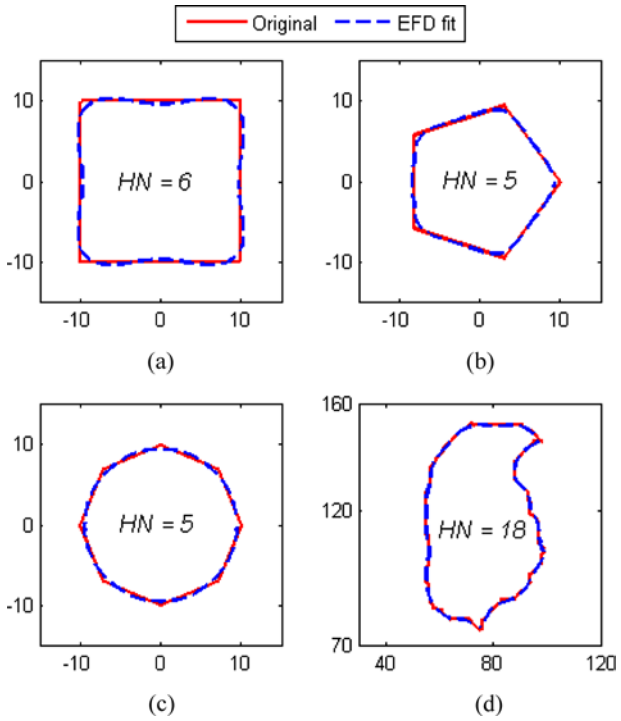

The result of the data manipulation stage is a point cloud of data representing planar section outlines of the object. This point cloud can be fit with a surface to produce a final 3D model.

Object reconstruction: Meshlab (2008) (Pisa, Italy), an "open source, portable, and extensible system for the processing and editing of unstructured 3D triangular meshes", was chosen as the surface reconstruction software for this scanner. Meshlab is capable of exporting the final 3D model into many different file formats making the final 3D model versatile and open to many different applications. For converting point clouds into triangulated 3D surface reconstructions, Meshlab implements the efficient ball-pivoting algorithm described by Bernardini et al. (1999). It should be noted that object reconstruction is not the main focus of this works. Consequently, the choice of using Meshlab may be sub-optimal, but was made for completeness with convenience in mind.

3 Methods

This section describes the methods for two experiments, which validate the proposed design. The first evaluates the effectiveness of EFDs for curve fitting at the data manipulation phase and also provides a quantitative assessment of system performance for a scanned cylinder of known dimensions. For the second experiment, two other objects were scanned with the system to provide more qualitative results; 3D models for these objects, as well as the cylinder from the previous experiment, were generated.

3.1 EFD analysis

To demonstrate the validity of our approach to curve fitting described in Section 2.3, a simulation was conducted whereby EFDs were used to fit a set of ideal input data with Additive White Gaussian Noise (AWGN). This would demonstrate the effectiveness of EFDs for reducing random noise in the absence of systemic noise. Random white Gaussian noise with zero mean and a variance of $\sigma^2 = 3.9 \times 10^{-3}$ was added to circle data with an ideal radius of $r = 9.525\,\text{mm}$ ($\frac{3}{8}$ in). The chosen variance is an estimate of the variance in the random noise observed in the data of previous experiments.

To demonstrate the effectiveness of using EFDs with data obtained from this system, an experiment was conducted to reconstruct a small portion of a cylinder test object. First, the DLT LS calibration procedure described in Section 2.3 was performed; 40 point correspondences were used to find H. Then, images for $N_z = 4$ planar sections of the test cylinder object with radius $r = 9.525\,\text{mm}$ ($\frac{3}{8}$ in) were captured. For each plane, $M = 8$ images of the laser trace on the object were captured in rotational increments of $R = 45°$. Planar sections were captured at 2 mm increments in the positive z-axis direction. In total, 32 images of laser trace segments were captured for reconstructing the four planar sections. For data processing, the procedure outlined in Section 2.3 was followed. In this case, only one harmonic was required to accurately fit the test cylinder object.

The final object contours were stacked along the reconstruction z-axis. Root Mean Squared (RMS) error in point location along the section outline for each planar section was calculated, where the error is the difference between the ideal radius and the distance to each point on the section's outline from the section centre. Error was calculated using the sections' respective centroids as the centre as well as the mean centroid location as the centre. This is to be able to asses the individual dimensional accuracy of sections (i.e., how close is each section to the ideal radius), as well as accuracy in the vertical direction (i.e., if sections are translated to a mean centroid location, how close is each section to the ideal radius).

3.2 Final 3D models

In addition to the test cylinder described in Section 3.1, 3D models were created for two other objects: an oval cap and a miniature arm model. Since the cap and arm were imaged during a different session, they required a new calibration; 42 point correspondences were used in this case for finding H. Images for $N_z = 10$ and $N_z = 20$ planar sections were captured for the cap and arm object, respectively. For each plane,

$M = 8$ images of the laser trace were captured in rotational increments of $R = 45°$. Planar sections were captured at 2 mm increments in the positive z-axis direction. For data processing, the procedure outlined in Section 2.3 was followed; the number of harmonics used for each of the EFD contours was computed according to equation (13) and the EFD reconstructions, consisting of 100 data points per contour, were stacked along the z-axis. 3D models of each object were generated from the resulting point clouds using Meshlab. Scan acquisition time and data processing time were recorded for each object.

Table 1 summarises the acquisition parameters for all the objects: namely, the approximate object volume, the number of calibration points used for computing H, the vertical resolution used for the scan, the number of sections captured and the number of points used for the EFD outlines.

Table 1 Summary of acquisition methods

Shape	*Approx. volume scanned* (mm^3)	*No. calibration points*	*Vertical resolution* (mm)	*No. of sections*	*No. points in EFD outline (per section)*
Cylinder	$9.5 \times 9.5 \times 8$	40	2	4	500
Oval cap	$13 \times 20 \times 20$	42	2	10	100
Model arm	$20 \times 25 \times 40$	42	2	20	100

4 Results

4.1 EFD analysis

Figure 6 shows the EFD fit for the simulated ideal circle data with AWGN. Figure 7 is a plot of the radii obtained from the reconstruction process of the test cylinder, both before and after the contour was fit with a smooth curve using the EFD technique. Only the first planar section is shown; however, results were similar for all four layers that were reconstructed for this experiment. As indicated, the ideal radius in this case was $r = 9.525$ mm ($\frac{3}{8}$ in). Table 2 shows the RMS error for all sections of the test cylinder when the radius of the section is calculated from both the sections' respective centroids and from the mean centroid. Figure 8 shows the four planar sections of the test cylinder, fitted using EFDs and scaled appropriately.

4.2 Final 3D models

It is difficult to quantify system accuracy for these objects without ground truth information; however, qualitative assessment is possible by examining the resultant 3D images. Figures 9–11 show images of the original objects, plots of the EFD planar section point clouds, and their 3D surface reconstructions, including the test cylinder discussed above. Table 3 summarises other results of interest for these objects: namely, the scan acquisition time, the number of harmonics calculated for the EFD fit, the number of vertices in the EFD point cloud, the

data processing time, and the number of faces in the final surface reconstruction. Scan time refers to the total time required for acquiring image data, including the time to rotate the object and increment the camera/laser platform. Data processing time refers to the CPU time for the computation of the EFD point cloud of planar

Figure 6 Profile of simulation data (circle with $r = 9.525$ mm). Radius shown as a function of theta from 0 to 2π for the noisy data before the EFD fit and after the EFD fit (see online version for colours)

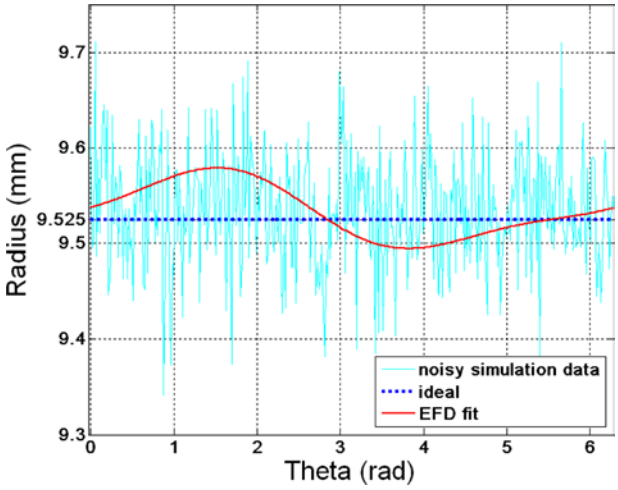

Figure 7 Profile of test object (cylinder with $r = 9.525$ mm). Radius shown as a function of theta from 0 to 2π for the raw data before the EFD fit (constructed from eight segments, S1–S8) and after the EFD fit (see online version for colours)

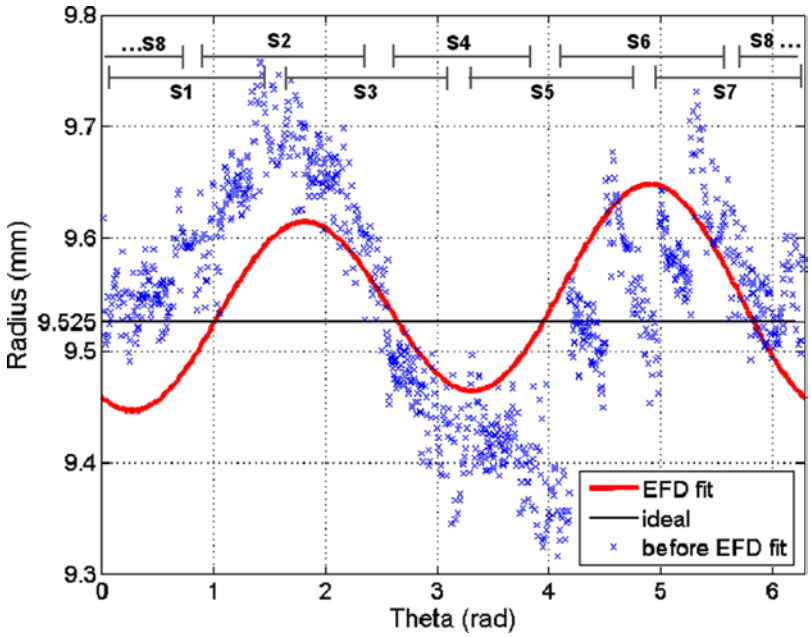

sections from the scan images, and does not include the surface mesh reconstruction in Meshlab. The system takes about 40 s to capture the eight images required for one planar section, the majority of which is mechanical rotation time of the object. Actual image acquisition with Labview takes between 500 ms and 600 ms per image, meaning that actual image acquisition time is only about 10% of the total scan time.

Table 2 RMS error for each planar section of the cylinder object before and after translating to the mean centroid

	RMS error (mm)	
Section	*Relative to section centroid*	*Relative to mean centroid*
1	0.0666	0.1235
2	0.2222	0.2245
3	0.0716	0.1076
4	0.0674	0.0861
Mean	*0.1069*	*0.1354*

Figure 8 Four reconstructed planar sections of a test cylinder fitted with EFDs (see online version for colours)

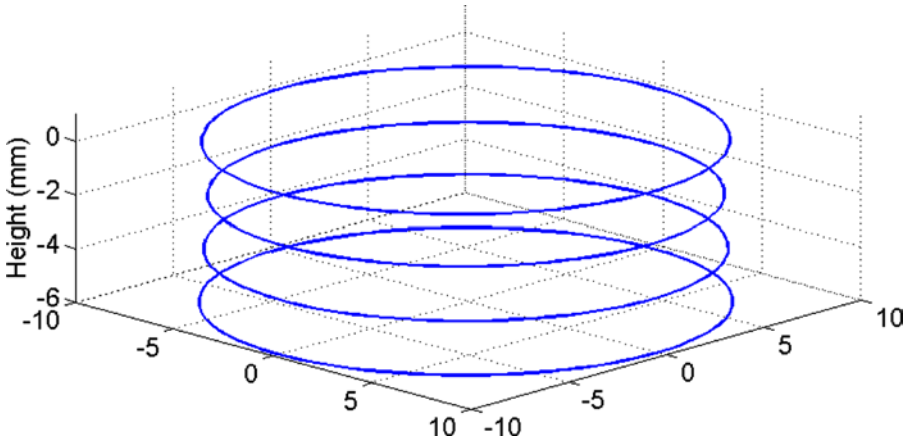

Figure 9 3D reconstruction of cylinder test object (see online version for colours)

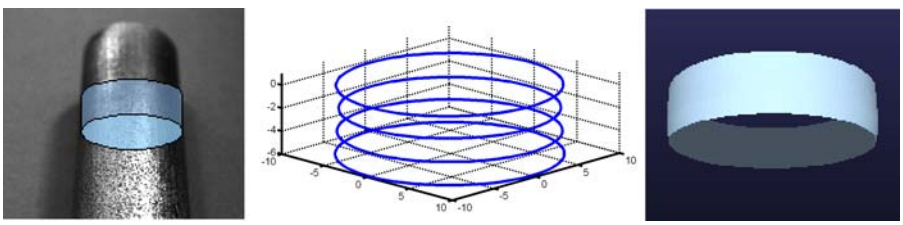

Figure 10 3D reconstruction of oval cap (see online version for colours)

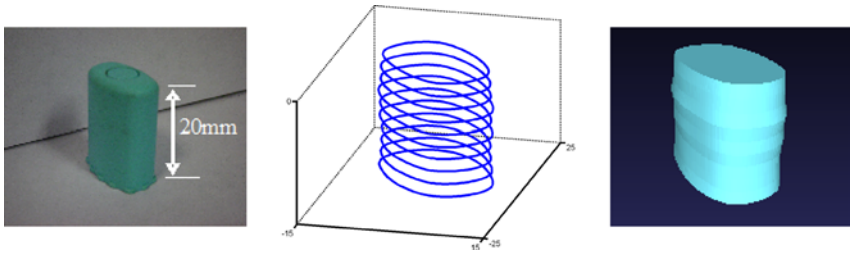

Figure 11 3D reconstruction of miniature arm model (see online version for colours)

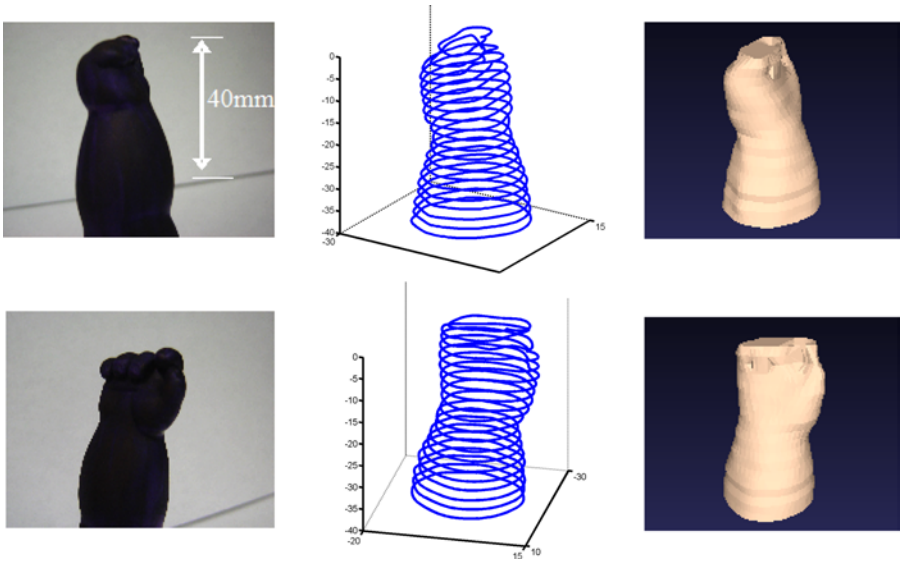

Table 3 Summary of scanned object results

Shape	*Scan time*	*No. of harmonics (range)*	*No. of vertices*	*Data processing time* (s)	*No. of faces*
Cylinder	2 mins 40 s	1	404	10.41	600
Oval cap	6 mins 40 s	5–6	1010	20.28	1894
Model arm	13 mins 20 s	5–8	2020	27.48	2053

5 Discussion

5.1 EFD analysis

For the simulated scenario shown in Figure 6 the noise is strictly random. The EFD fit provides a marked improvement over the noisy data; error does not exceed 0.1 mm in this case. A sinusoidal shape exists, which means the EFD fit is slightly

offset from the origin. The origin of the EFD is determined by the coefficients A_0 and C_0 which are essentially the mean of all the input data points (i.e., the centroid of input points). Therefore, any result other than $(0, 0)$ for the centroid will result in A_0 and C_0 not equal to zero, and hence a slightly shifted fit. Although the added noise had zero mean in theory, it is unlikely that the mean of all points was exactly zero for this simulation. Overall, this offset is very small.

As shown in Figure 7, the registered and averaged segments for the given planar section of the test cylinder appear to produce a fairly good result, even before a curve was fit to the data with the EFD technique. Errors do not exceed 0.25 mm. Although sub-mm accuracy is achieved overall, there is observable noise in the error plot (Figure 7). This noise appears to be made up of mostly random noise. This random error could be due to noise inherent in the measurement system and noise in the resulting point coordinates obtained from the COG algorithm. The subsequent EFD contour for this first layer shows a fairly close fitting through the points using only one harmonic. Random noise is clearly attenuated in the EFD fit, and overall error is also reduced. RMS error for this section is 0.1235 mm from the mean centroid location. The sinusoidal shape observed in Figure 6 is also present in Figure 7, both before and after the data are fit with EFDs. As with the simulation results, reasons for this offset are due to the A_0 and C_0 terms of the EFD outlines being the mean of input data, thus centering the EFD contour at this mean. Since the mean of input data is not necessarily equal to the centroid of the resulting EFD fit, calculating the radius from this point would result in a slight offset and hence the sinusoidal shape.

As shown in Table 2, mean RMS error across all sections is 0.1354 mm. Although each radius profile is quite close to the ideal value, there are some slight issues of scale across sections, particularly for Section 2 which has the highest RMS error ($\sim$0.2 mm) of all sections captured. Possible sources for this could be due to the apparatus setup. Although the camera and laser are fixed to a platform, and ideally fixed relative to each other, slight deviations in the horizontal alignment of the laser plane with respect to the xy-plane would change the laser profile on the object, and would thus propagate through the data processing as an error in overall scale. Instability of the platform could be the cause of the scaling issues. Visual inspection of the reconstructed planar sections of the test cylinder (Figure 8) reveals that the proposed approach can produce a planar section model, which is reasonably complete in desired external detail.

In summary, the data presented shows the advantage of using EFDs for fitting a contour through the segment data obtained from the laser light-sectioning technique. Although the EFD technique does not provide a substantial improvement in overall accuracy, random error is attenuated considerably, resulting in a smooth curve that closely matches the dimensions of the object of interest.

5.2 Final 3D models

Although no exact value of accuracy can be provided for the other objects scanned, visually, the EFD planar section models and their respective 3D models (Figures 10 and 11) are reasonably complete in external detail. There still exists slight variation in scale across sections, as shown by the bumpiness in the rendered 3D models; however, these objects are quite small and these errors are still within an acceptable tolerance for this system. The miniature arm model lacks detail in the hand region.

This is mostly attributed to the limited vertical resolution of the scan (2 mm increments), resulting in triangulation which spans across gaps existing on the real model. This also accounts for the flat surface on top; the next highest planar section image contained no light reflections. The system does have the capability of scanning with finer vertical resolution; however, this has yet to be tested.

Since it takes a fixed amount of time to capture a section, scan time increases when more planar sections are captured, regardless of object complexity. With improvements in the overall mechanical design, scan time can be reduced significantly; it is currently limited by the mechanical movements of the apparatus, not acquisition speed.

Given these results, the method for choosing an appropriate number of harmonics appears to be promising; however, more work is needed to properly validate and quantitatively assess the approach. Overall, these results are considered to be quite good considering the low-cost components which have been used for this setup.

Current limitations of the system lie mostly with the mechanical setup, and include servo motor rotation accuracy, structural stability, overall scan time, and the general need to rotate the object rather than rotate the camera/laser about the object. The volume of objects which can be scanned is currently quite small, a limitation which can be rectified with a different zoom setting on the camera. Also, although the collection of raw data for objects with discontinuous profiles (i.e., the finger area of an open hand or an object with a hole through it) is possible with the current system (because images are captured from many different views), additional data processing would be required to represent such surfaces with EFDs. As with all systems employing the laser light-sectioning technique, both the camera and the laser require a direct line of sight to the object's surface in order to capture surface data. This poses a limitation when it comes to objects with concavities or hollow interiors. Improving these aspects of the current design are topics for future work.

6 Conclusion

The accuracy results presented for the test cylinder object are considered to be well within the realm of acceptability for biomedical applications. The sub-mm accuracy achieved compares well with laser light-sectioning systems in the literature, as well as some commercial systems. Given the low cost components used and current limitations of the mechanical setup, increased accuracy is anticipated with future refinements in the system.

As the system exists now, potential applications would be scanning of inanimate, but still anatomical-like objects, which can be placed on a turntable and scanned, such as a hearing aid shell or dental model. This was demonstrated by the arm model experiment, which had anatomical-like features. A desired feature of the proposed system will be the ability of the camera and laser system to rotate about an object with the required number of degrees of freedom making it flexible for numerous applications. This is particularly important for biomedical applications where the apparatus would ideally rotate about a patient and not vice versa. This, along with an improved mechanical setup, are topics for future work.

Overall, by including more complexity in signal processing and analysis, we were able to use simple, inexpensive, off-the-shelf components in a straight-forward

setup avoiding complex optical schemes. Specifically, the calibration process chosen avoids the need to explicitly calculate extrinsic or intrinsic camera parameters or precise component orientations. Imperfections in alignment will be quantified and compensated for by the transformation matrix H found through the calibration procedure. Automation of the image acquisition process is also an important feature of the design, to help reduce the need for user intervention. The straightforward data collection setup allows for the segments to be easily registered into the proper coordinate system based on object rotations and camera/laser increments. The applicability of EFDs for curve fitting has been demonstrated; by choosing this approach we are specifically addressing noise in the measurement data with a technique particularly suited for modelling biological objects.

Acknowledgements

This work was supported in part by a grant from the National Science and Engineering Research Council (NSERC). Paul O'Leary (Institute for Automation, University of Leoben, Leoben, Austria) and M. John D. Hayes (Mechanical and Aerospace Engineering, Carleton University) are acknowledged for the partial use of their Matlab code for some of the data processing steps.

References

Azouz, Z.B., Shu, C., Lepage, R. and Rioux, M. (2005) 'Extracting main modes of human body shape variation from 3D anthropometric data', *Proc. 5th Int'l Conf. 3-D Digital Imaging and Modeling*, Ottawa, Ont., Canada, pp.335–342.

Bernardini, F., Mittleman, J., Rushmeier, H., Silva, C. and Taubin, G. (1999) 'The ball-pivoting algorithm for surface reconstruction', *IEEE Trans. Visualization and Computer Graphics*, Vol. 5, No. 4, pp.349–359.

Bernardini, F. and Rushmeier, H. (2002) 'The 3D model acquisition pipeline', *Computer Graphics Forum*, Vol. 21, No. 2, pp.149–172.

Boehnen, C. and Flynn, P. (2005) 'Accuracy of 3D scanning technologies in a face scanning scenario', *Proc. 5th Int'l Conf. 3D Digital Imaging and Modeling*, Ottawa, Ontario, Canada, 13–16 June, pp.310–317.

Bradley, B.D., Chan, A.D.C. and Hayes, M.J.D. (2008) 'Calibration of a simple, low cost, 3D laser light-sectioning scanner system for biomedical purposes', *Proc. 31st Annual Canadian Medical and Biological Engineering Conference, CMBEC31*, June, Montréal, Canada, Paper A10-3, pp.1–4.

Curless, B. (1999) 'From range scans to 3D models', *Computer Graphics*, Vol. 33, No. 4, pp.38–41.

Hajeer, M.Y., Millett, D.T., Ayoub, A.F. and Siebert, J.P. (2004) 'Applications of 3D imaging in orthodontics: Part I', *J. Orthodontics*, Vol. 31, pp.62–70.

Hayes, M.J.D., Leitner, M., O'Leary, P., Ofner, R. and Sallinger, C. (2001) 'An integrated optical-robotic measurement system', *Proc. 8th Canadian Congress of Applied Mechanics (CANCAM '01)*, St. John's, Canada, pp.287–288.

Hennessy, R.J., McLearie, S. and Kinsella, A. (2005) 'Facial surface analysis by 3D laser scanning and geometric morphometrics in relation to sexual dimorphism in cerebral-craniofacial morphogenesis and cognitive function', *J. Anatomy*, Vol. 207, No. 3, pp.283–295.

Jeong, Y. and Radke, R.J. (2007) 'Reslicing axially sampled 3D shapes using elliptic Fourier descriptors', *Medical Image Analysis*, Vol. 11, pp.197–206.

Kovacs, L., Zimmermann, A., Brockmann, G., Baurecht, H., Schwenzer-Zimmerer, K., Papadopulos, N.A., Papadopoulos, M.A., Sader, R., Biemer, E. and Zeilhofer, H.F. (2006) 'Accuracy and precision of the three-dimensional assessment of the facial surface using a 3D laser scanner', *IEEE Trans. Medical Imaging*, Vol. 25, No. 6, pp.742–754.

Khul, F.P. and Giardina, C.R. (1982) 'Elliptic Fourier features of a closed contour', *Computer Graphics and Image Processing*, Vol. 18, pp.236–258.

Lestrel, P.E. (Ed.) (1997) *Fourier Descriptors and their Applications in Biology*, Cambridge University Press, Cambridge.

Lichtschnitt, A. (2004) *Laser Light Section: A Key Feature in 3D Laser Measurement Technique*, Schafter and Kirchhoff, Hamburg, Germany, Obtained through the Internet: http://www.sukhamburg.de/dl/lightsect-e.pdf, Accessed: 29 June.

Meshlab (2008) *Visual Computing Lab*, Italian National Research Council, Obtained through the Internet: http://meshlab.sourceforge.net, Accessed: 22 May.

Ofner, R., O'Leary, P. and Leitner, M. (1999) 'A collection of algorithms for the determination of construction points in the measurement of 3D geometries via light-sectioning', *2nd Workshop on European Scientific and Industrial Collaboration Promoting: Advanced Technologies in Manufacturing*, Newport, South Wales, UK, pp.505–512.

Otsu, N. (1979) 'A threshold selection method from gray-level histograms', *IEEE Transactions on Systems, Man, and Cybernetics*, Vol. 9, No. 1, pp.62–66.

Rutishauser, M., Sticker, M. and Trobina, M. (1994) 'Merging range images of arbitrarily shaped objects', *Proc. IEEE Conf. Computer Vision and Pattern Recognition*, Seattle, Washington, pp.573–580.

Schmittbuhl, M., Le Minor, J-M., Schaaf, A. and Mangin, P. (2002) 'The human mandible in lateral view: elliptical fourier descriptors of the outline and their morphological analysis', *Annals of Anatomy*, Vol. 184, pp.199–207.

Schwenzer-Zimmerer, K., Haberstok, J., Kovacs, L., Boerner, B.I., Schwenzer, N., Juergens, P., Zeilhofer, H-F. and Holberg, C. (2008) '3D surface measurement for medical application-technical comparison of two established industrial surface scanning systems', *J. Med. Sys.*, Vol. 32, pp.59–64.

Soucy, M. and Laurendeau, D. (1995) 'A general surface approach to the integration of a set of range views', *IEEE Trans. Pattern Analysis and Machine Intelligence*, Vol. 17, No. 4, pp.344–358.

Tognola, G., Parazzini, M., Ravazzani, P., Grandori, F. and Svelto, C. (2003a) '3D acquisition and quantitative measurements of anatomical parts by optical scanning and image reconstruction from unorganized range data', *IEEE Trans. Instrum. Meas.*, Vol. 52, No. 5, pp.1665–1673.

Tognola, G., Parazzini, M., Svelto, C., Ravazzani, P. and Grandori, F. (2003b) 'A fast and reliable system for 3D surface acquisition and reconstruction', *Image and Vision Computing*, Vol. 21, pp.295–305.

Trinh, N.H., Lester, J., Fleming, B.C., Tung, G. and Kimia, B.B. (2006) 'Accurate measurement of cartilage morphology using a 3D laser scanner', *Proc. 2nd Int'l ECCV Workshop on Computer Vision Approaches to Medical Image Analysis*, Graz, Austria, pp.37–48.